

On rotating thermal convection driven by non-uniform heating from below

By PHILLIP HIGNETT,

Meteorological Office, Bracknell, Berkshire

ALAN IBBETSON

Department of Meteorology, University of Reading

AND PETER D. KILLWORTH

Department of Applied Mathematics and Theoretical Physics,
University of Cambridge

(Received 25 February 1980 and in revised form 14 November 1980)

Experiments are described in which a radial temperature gradient is maintained along the lower horizontal boundary of a rotating annulus containing a thermally convecting fluid; the vertical side walls and upper horizontal boundary are nominally insulating. Comparison is made with the non-rotating experiments of Rossby (1965) and the same general asymmetric circulation is observed, i.e. that of a weakly stratified interior of slowly descending fluid occupying most of the annular gap, overlying a thin thermal layer of large vertical temperature gradients, stable over the cold part of the base and statically unstable over the warmer part; the circulation is completed by a narrow region of rising motion at the warm end of the base.

A boundary-layer scaling analysis demonstrates the existence of six flow regimes, depending on the magnitude of a quantity Q defined such that Q is the square of the ratio of the (non-rotating) thermal-layer scale to the Ekman-layer scale. For small Q the flow is only weakly modified by rotation but as Q increases past unity rotation tends to thicken the thermal layer. Also presented are some numerical similarity solutions for the special case of a quadratic temperature distribution on the lower boundary and partially covering the range of Q achieved in the experiments, which is zero to ten. Above a certain critical value of Q (for the geometry used here $Q_c = 3.4$) a baroclinic wave regime exists but is not examined in detail here although a brief discussion of an instability problem is given. Throughout comparisons are drawn between the experimental results and theoretical aspects of the problem.

It is thought that the essential features of a system thermally driven in this way have their counterparts in natural systems such as the large-scale thermally induced ocean circulation driven by the latitudinal variation of incoming solar radiation.

1. Introduction

Laboratory experiments have an established role in many aspects of geophysical fluid dynamics; the present experiments are concerned with the effects of rotation on a thermally convecting fluid which is heated and cooled along a horizontal boundary, all other boundaries being considered as nominally insulating. The original stimulus

was essentially an oceanographic one concerned with the strongly asymmetric nature of the general ocean circulation, characterized by narrow regions of downwelling at high latitudes, where there is a net cooling, and a slow upwelling elsewhere.

Despite the objections of Jeffreys (1925), the remarks of Sandström (1908) and Bjerknes (1916) denying that a significant thermal circulation can be driven by a distribution of heat sources and sinks on a horizontal boundary gained some acceptance (e.g. Defant 1961). Stommel (1950, 1962) interpreted the essential asymmetry of the problem on the basis of a simple theoretical model; this led to the successful demonstration of the asymmetry in the non-rotating laboratory experiments of Rossby (1965). Rossby used a rectangular tank with insulating upper walls and maintained a linear temperature gradient along the lower boundary. The resulting picture was of a thin strongly stratified thermal layer over the base with the flow directed towards the hot end of the cell and feeding into a narrow rising plume. The interior was weakly stably stratified and attained a temperature equivalent to about 70 % of the applied temperature difference. Rossby explained the asymmetry as a consequence of the relative efficiencies of convective and conductive heat transport. All heat must enter and leave through the base, thus warming the interior advectively and maintaining an overall balance by conduction to the base. Rossby was able to estimate the heat flux and circulation strength and found these values compared favourably with his scaling analysis. Similar unpublished experiments by Miller (1968), performed with a saw-tooth form of lower-boundary temperature gradient, to remove the influence of the side wall from the plume, exhibited the same general characteristics.

There have been several relevant analyses of both rotating and non-rotating systems. The most recent non-rotating study, that of Killworth & Manins (1980) was prompted by Rossby's experiments and the numerical study of Beardsley & Festa (1972). Killworth & Manins derive a similarity solution for the boundary layer under the condition of a parabolic distribution of buoyancy on the base. Stern (1975) and Daniels (1976) have made theoretical studies, in restricted parameter regimes, of the flow in a narrow-gap rotating annulus driven by a specified temperature distribution on the lower boundary. A scaling analysis which effectively defines the various flow regimes for the rotating problem is presented in §3 and establishes the range of validity of Stern and Daniels' analyses. Section 5 extends the similarity solution of Killworth & Manins to the rotating case.

In the controlled experimental work described here the working fluid was contained in the annular gap between two vertical concentric cylinders rotating about their common axis. The side walls and lid were nominally insulating and a radial temperature was maintained along the base. This, of course, differs from the traditional annulus experiments, in which a horizontal temperature gradient is maintained by differentially heating the side walls. Such systems have been the subject of intensive investigations (e.g. Hide 1969; Hide & Mason 1975) and many features of rotating, baroclinic flows have been elucidated in this way. It was the intention of the present experiments to establish the controlling external parameters whilst concentrating attention on the structure of the thermal boundary layer and characteristic features such as the variation of the temperature of the interior region and the heat transport. Details of the apparatus and techniques can be found in §2. The experimental results are presented in §4, in which it will be seen that the rotating flows preserve the same essential characteristics as the non-rotating flow but a new feature arises when the baroclinic azimuthal

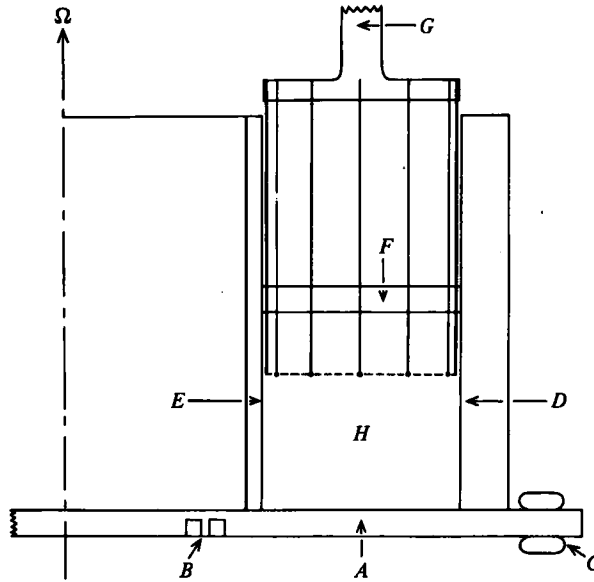


FIGURE 1. A schematic cross-section through the annulus. The labelled features are: *A*, copper base; *B*, cold water channels; *C*, warm water coils; *D*, outer cylinder; *E*, inner cylinder; *F*, lid; *G*, thermocouple array; *H*, convection chamber. The thermocouple positions are labelled *I* to *V* and are positioned radially at $r = a + (0.07, 0.25, 0.50, 0.72, 0.92)(b - a)$.

flow induced by the rotation becomes unstable and exhibits a wave flow similar to that observed in the side-wall heated annulus. A detailed analysis of the structure of these waves and their influence on the basic flow should be the subject of future study and only a few largely qualitative comments can be made here.

2. Experimental apparatus

Two fluids were employed in the experiments, water and paraffin. The properties of water are well tabulated; the relevant properties of the samples of paraffin used, at 20 °C, are $\alpha = (9.4 \pm 0.3) \times 10^{-4} \text{ K}^{-1}$, $\nu = 1.82 \times 10^{-2} \text{ cm}^2 \text{ s}^{-1}$ ($\pm 5\%$) and $\kappa = 1.1 \times 10^{-3} \text{ cm}^2 \text{ s}^{-1}$ ($\pm 10\%$). The working fluid was contained in the annular gap between two concentric acrylic cylinders, the outer of inner radius $b = 20.3 \text{ cm}$ and thickness 2.54 cm, and the inner of outer radius $a = 10.0 \text{ cm}$ and thickness 1 cm. The inner cylinder was filled with insulating polystyrene foam. The lid was of 1 cm thick acrylic sheet and was in contact with the fluid; for most experiments the depth was fixed at 10 cm. The gap width, $(b - a)$, was fixed at a value of $10.3 \pm 0.05 \text{ cm}$ for most of the experiments. The cylinders were secured to a copper disk, thickness 0.95 cm, along which a radial temperature gradient could be maintained by circulating water through copper coils soldered to the rim and channels cut inward of the inner cylinder. Conventionally $T(b) > T(a)$ and once established the temperature difference defined by the positions of the side walls was found to be constant to $\pm 0.05 \text{ K}$ over periods of several hours. Because of the curvature the base temperature was approximated by $T(r, 0) = T(a) + \Delta T \ln(r/a) / \ln(b/a)$. It was intended that the heat flux through the base be much greater than that through the fluid in order to decouple the lower boundary

<i>a</i>	radius of inner cylinder
<i>b</i>	radius of outer cylinder
<i>d</i>	depth of fluid
<i>r</i>	distance from rotation axis
<i>Z</i>	height above annulus base
<i>u</i>	radial velocity component, positive outwards
<i>v</i>	azimuthal velocity component, positive anticlockwise
<i>w</i>	vertical velocity component, positive upwards
<i>h</i>	thermal layer depth
δ	Ekman layer depth = $(\Omega/\nu)^{1/2}$
ρ	fluid density
<i>T</i>	fluid temperature
ΔT	maximum imposed temperature difference on the base
\bar{T}	mean applied temperature = $\frac{1}{2}(T(a) + T(b))$
Ω	rotation rate
<i>g</i>	acceleration due to gravity
α	coefficient of thermal expansion
ν	kinematic viscosity
κ	thermal diffusivity
<i>J</i>	Jacobian operator, $J(a, b) = \frac{\partial a}{\partial x} \frac{\partial b}{\partial z} - \frac{\partial a}{\partial z} \frac{\partial b}{\partial x}$
<i>Ra</i>	Rayleigh number = $g\alpha\Delta T(b-a)^3/\nu\kappa$
<i>E</i>	Ekman number = $\nu/2\Omega(b-a)^2$
σ	Prandtl number = ν/κ
<i>Nu</i>	Nusselt number = ratio of total heat transfer to that accomplished by a solid with the same thermal properties.
<i>Q</i>	$(R^{-1/2}/E^{1/2})^2 = 2\Omega(b-a)^{5/2}\kappa^{1/2}/(g\alpha\Delta T)^{1/2}\nu^{1/2}$

TABLE 1. Notation and dimensionless parameters. Experimentally the non-dimensional parameters were worked out using values of the fluid physical properties appropriate to the temperature \bar{T} . A schematic representation of the apparatus is given in figure 1.

condition from fluid motions; it is estimated that the fluid heat flux was always < 10% of that through the base.

The annulus was levelled (to within 10^{-4} radians) and centred on a turntable driven directly by a servo-controlled permanent magnet d.c. motor. Long-term stability of the rotation rate (over several hours) was one part in 10^3 and short-term stability (a few tens of rotation periods) one part in 10^4 . For these experiments the rotation rate was conveniently varied over the range 0.1 to 2 radians per second, the upper limit ensuring that the geopotentials remain almost parallel to the end walls. The maximum temperature difference which could be maintained across the gap width of 10.3 cm was ≈ 15 K.

Temperatures were measured by copper-constantan thermocouples, which have a sensitivity of $\approx 40 \mu\text{V K}^{-1}$; to establish the base temperature distribution thermocouple junctions made from $125 \mu\text{m}$ wire were buried in tightly fitting holes arranged in a spiral in the underside of the base, giving a radial spacing of approximately one junction per centimetre. Fluid temperatures were measured using a thermocouple array formed by stretching a single horizontal $50 \mu\text{m}$ constantan wire radially between two vertical supports made from 0.05 cm diameter hypodermic needles. Vertically hung $50 \mu\text{m}$ copper wires were soldered at intervals to form junctions at five radial positions. The upper ends of the supports and wires were held in an acrylic block capable of being moved up or down by means of a stepper-motor-driven screw thread.

The array was dipped into the fluid through a narrow slot in the lid; repeatability of positioning was better than 0.01 cm. A schematic cross-section of the annulus including the relative position of the thermocouple and the spacing of the junctions is shown in figure 1.

To help approximate insulating boundary conditions the near-isothermal state of much of the fluid was exploited. The annulus, turntable and all attendant low-level signal cables were contained within an enclosure whose air temperature could be maintained at a value which would minimize the temperature difference across the side walls and lid. This also aided the stability of the electrical system, which was such that although the absolute accuracy of a single measurement was ± 0.05 K the scatter in measurements made when the fluid was isothermal was $< \pm 0.01$ K over periods of about an hour.

Flow visualization and some velocity measurements were accomplished using the thymol blue indicator technique described by Baker (1966), which is suitable of course for use only in aqueous solutions. A single horizontal $75 \mu\text{m}$ diameter copper wire was stretched radially between two vertical supports which were attached to the probe positioner normally used for thermocouple measurements. Sections of the wire were left uninsulated, enabling a qualitative investigation of the flow at different levels and some direct measurements via sequences of photographs taken by a remotely controlled motor-driven 35 mm camera attached to a tripod mounted on the turntable.

3. Boundary-layer scalings and parameter ranges

The experimental work described in later sections deals with the flow in an annulus of which the outer cylinder has radius $b = 20.3$ cm and the inner cylinder (in most experiments) radius $a = 10.0$ cm. In this section an idealized problem is considered in which curvature is neglected and the side and upper boundaries are taken as perfectly insulating. This neglect of curvature requires that the gap width of the annulus be much less than the mean radius, i.e. that the quantity $2(b-a)/(b+a)$ be much less than 1. In practice this had a value of ~ 0.68 , except in a very few experiments with a larger inner cylinder (to give $(b-a) = 5$ cm) when it was reduced to ~ 0.4 . Furthermore it is experimentally difficult to achieve perfectly insulating boundary conditions, although attention was given to minimizing the temperature difference across the side walls and lid. Thus it is not possible, in general, to make direct comparison between experiment and an idealized study, although the latter is capable of describing the characteristic features and in particular their dependence on the impressed parameters, such as the temperature difference and rotation rate.

The system is defined by four non-dimensional parameters. These are the 'horizontal' Rayleigh and Ekman numbers, Ra and E , Prandtl number σ , and an aspect ratio, depth \div width, normally assumed to be of order unity. Notation and the definition of various non-dimensional numbers, as used experimentally, are summarized in table 1. The Boussinesq equations of motion for steady, two-dimensional incompressible flow, neglecting curvature and assuming density to be a linear function of temperature, may be written as (with letters identifying terms for later convenience): the vorticity equation

$$\nu \nabla^4 \psi = \Delta x - 2\Omega v_z - J(\psi, \nabla^2 \psi) \quad (3.1)$$

$$[A = B + C + D];$$

the buoyancy (or heat) equation

$$\begin{aligned} \kappa \nabla^2 \Delta &= -J(\psi, \Delta) \\ [E &= F]; \end{aligned} \quad (3.2)$$

and the azimuthal momentum equation

$$\begin{aligned} \nu \nabla^2 v &= 2\Omega \psi_z + J(v, \psi) \\ [G &= H + I]. \end{aligned} \quad (3.3)$$

Here suffixes denote differentiation, ψ is a stream function defined so that $u = \psi_x$, $w = -\psi_z$, and Δ is the buoyancy $g\alpha(T - T_c)$ relative to the coldest part of the fluid, of temperature T_c . The relevant boundary conditions are a specified buoyancy distribution on the (rigid) base, and rigid, insulating vertical side walls and horizontal lid. In this system the Rayleigh and Ekman numbers are now $Ra = \Delta_m L^3 (\nu \kappa)^{-1}$ and $E = \nu (2\Omega L^2)^{-1}$, where Δ_m is the maximum imposed buoyancy difference and L is a horizontal length scale. For the annulus this can be identified with the gap width $(b - a)$.

Rosby (1965) demonstrated that the horizontal thermal layer has a non-dimensional thickness $Ra^{-\frac{1}{2}}$, when Ra is large, in the non-rotating case. In a homogeneous rotating system, however, the thinnest horizontal boundary layer is an Ekman layer, of non-dimensional thickness $E^{\frac{1}{2}}$ (e.g. Fein 1978), when E is small. It might thus be anticipated that the ratio of these two small quantities will be of importance in describing the flow. This turns out to be the case. We define the parameter

$$Q = (Ra^{-\frac{1}{2}}/E^{\frac{1}{2}})^2,$$

which has the convenient property that Q is a linear function of the rotation rate.

Using straightforward scaling analyses it appears that the system can be divided into six regimes depending mainly on the magnitude of Q and only weakly on the other parameters. For a fixed, large Rayleigh number (and assuming σ to be fairly large) these six regimes can be written as:

- (i) no rotation, $Q = 0$;
- (ii) very weak rotation, $Q \ll \sigma^{-1} \ll 1$;
- (iii) weak rotation, $\sigma^{-1} \ll Q \ll 1$;
- (iv) medium rotation, $Q \sim 1$;
- (v) strong rotation, $1 \ll Q \ll Ra^{\frac{4}{5}}$;
- (vi) very strong rotation, $Ra^{\frac{4}{5}} \ll Q$;

and their vertical structures are discussed briefly in turn. We defer consideration of the side-wall layers until later.

(i) The non-rotating case has been dealt with by Killworth & Manins (1980), who also obtained similarity solutions for the case of a parabolic distribution of buoyancy on the base. The stream function ψ is $O(\sigma^{\frac{1}{2}} \kappa Ra^{\frac{1}{2}})$ in the interior of the fluid, which is homogeneous, with a uniform buoyancy which depends on the details of the imposed buoyancy at the base. In the interior, vorticity $\nabla^2 \psi$ is a function of the stream function. There are two horizontal boundary layers on the base. The thicker is a dynamic homogeneous layer of non-dimensional thickness $\sigma^{\frac{1}{2}} Ra^{-\frac{1}{2}}$ in which the viscous term (A) balances advection of vorticity (D) and brings ψ to zero (a similar layer occurs at the lid). In the thinner, buoyancy layer, of non-dimensional thickness $Ra^{-\frac{1}{2}}$, ψ is reduced

by a factor $\sigma^{\frac{1}{2}}$. The balance is then $A \sim B$, $E \sim F$, so that this layer reduces Δ to its uniform interior value Δ_I by a balance of advection and diffusion of buoyancy.

(ii) As Q increases from zero but remains smaller than σ^{-1} , the very weak regime is entered. The azimuthal velocity v is of order $2\Omega L$, and the Taylor–Proudman theorem holds in the homogeneous interior ($v_z = u = 0$). At the lid there are two horizontal layers. The thicker ($\sim L Ra^{-\frac{1}{2}} \sigma^{-\frac{1}{2}} Q^{-1}$) reduces the size of ψ to $\nu Ra^{\frac{1}{2}} Q^{\frac{1}{2}}$, by nonlinear balances $C \sim D$, $H \sim I$, which then permits a thinner, traditional Ekman layer to bring ψ and v to zero. At the base, the dynamic and buoyancy layers remain, with v passively advected and diffused by the zonal flow ($G \sim H$, I ; $A \sim D$) in the dynamic layer, and vanishing in the buoyancy layer.

(iii) Increasing Q into the weak regime rescales v and ψ to $\kappa Ra^{\frac{1}{2}} L^{-1}$, $\kappa Ra^{\frac{1}{2}} Q^{-\frac{1}{2}}$ respectively. Thus v and u are the same order of magnitude, and at the lid there is only a simple Ekman layer. The interior remains homogeneous, with $u = v_z = 0$ as before. At the base the dynamic layer is replaced by another Ekman layer, much thicker (as Q is small) than the thermal layer, which retains the non-rotating form. The Ekman layer brings ψ and v to zero, and ψ_z is continuous between Ekman and thermal layers. Consequently the thermal layer depth h and Nusselt numbers are of the same order as found by Rossby (1965) and Killworth & Manins (1980):

$$h \sim L Ra^{-\frac{1}{2}} \quad \text{and} \quad Nu \sim Ra^{\frac{1}{2}}.$$

(iv) When Q becomes order unity (medium rotation) the thermal and Ekman layers at the base merge; this regime will turn out to be relevant for the experiments and the similarity solutions of §5. The appropriate non-dimensionalization for the thermal/Ekman layer are $\psi = \kappa Ra^{\frac{1}{2}} \psi'$, $v = \kappa Ra^{\frac{1}{2}} L^{-1} v'$, $\Delta = \Delta_m \Delta'$, $x = Lx'$, $z = L Ra^{-\frac{1}{2}} \zeta$ and, dropping primes, (3.1)–(3.3) become

$$\psi_{\zeta\zeta\zeta\zeta} = \Delta_x - Q v_{\zeta} + O(\sigma^{-1}), \quad (3.4)$$

$$\Delta_{\zeta\zeta} = -J(\psi, \Delta), \quad (3.5)$$

$$v_{\zeta\zeta} = Q \psi_{\zeta} + O(\sigma^{-1}), \quad (3.6)$$

together with a homogeneous interior and Ekman layer at the lid. Heuristically it can be seen from (3.4) to (3.6) that the thermal layer, when Q is still fairly small, will be affected by rotation at only large values of ζ . As Q increases, the increased Ekman spiral tendency produces a reduction in the size of ψ , and a corresponding increase in the thermal-layer thickness (as Δ decays more slowly). Hence the Nusselt number, formally $Nu = Ra^{\frac{1}{2}} f(Q)$ for some function $f(Q)$, will tend to decrease with increasing Q . The reduction in the rate of decay of Δ with ζ , as Q increases, similarly suggests that the abyssal buoyancy Δ_I should increase with Q . Finally, inspection of the ‘thermal wind’ balance $B \sim C$ indicates that v will decrease with increasing Q for large enough Q , from which it follows that v should reach a maximum for $Q \sim 1$.

(v) As Q becomes larger the Ekman layer lies well within the thermal layer, thus removing the frictional constraint of the lower boundary from the thermal layer, and establishing a ‘thermal wind’ balance $B \sim C$. This strongly rotating regime was discussed by Stern (1975) and Daniels (1976) and is the only case for which a non-similarity solution is known.† The interior balances, and the Ekman layer at the lid,

† Stern’s solution reduces to the similarity solution for quadratic buoyancy forcing at the base.

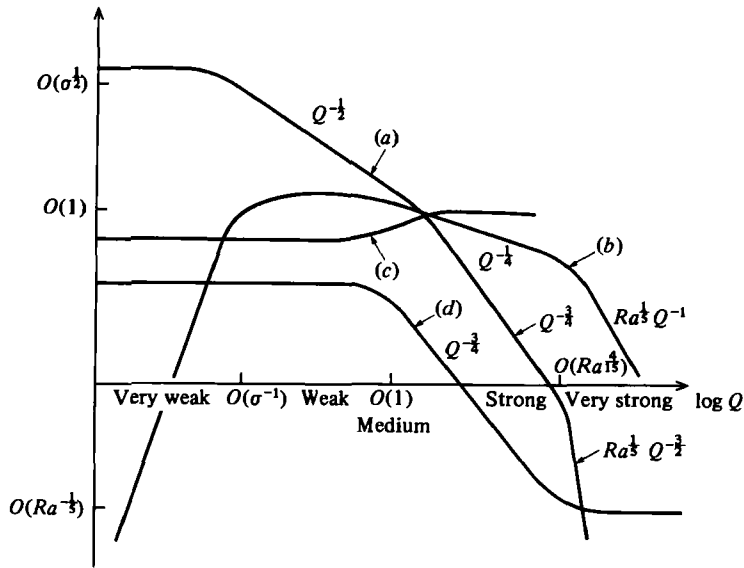


FIGURE 2. Schematic variation of quantities as Q varies, on log-log plot. Shown are (a) $\psi/\kappa Ra^{1/2}$; (b) $vL/\kappa Ra^{1/2}$; (c) $\Delta_I/\Delta_0(L)$; (d) $NuRa^{-1/2}$. In cases (a) and (b) the interior values are shown.

remain unchanged. Compatibility between upper and lower Ekman layers forces a reduction in the magnitudes of ψ and v , to $\kappa Ra^{1/2} Q^{-1/2}$, $\kappa Ra^{1/2} Q^{-1/2} L^{-1}$ respectively. This yields a much wider thermal layer, with thickness $h \sim L Ra^{-1/2} Q^{-1/2}$ and correspondingly $Nu \sim Ra^{1/2} Q^{-1/2}$. The dynamics of the lower Ekman layer are essentially homogeneous, although this narrow layer can and does change the vertical buoyancy gradient Δ_z . The interior buoyancy Δ_I is now the maximum value applied to the base (plus a term of order $Q^{-1/2}$). This had been assumed by Stern (1975) but can be derived from the theory.

(vi) Further increase in Q (to the very strong regime) extends the thermal layer beyond the depth of the annulus, a situation studied by Daniels (1976) in which the temperature field satisfies Laplace's equation and consequently $Nu = 1$. This is the only regime in which the interior is not homogeneous. ψ and v are still smaller; $\psi \sim \kappa Ra^{1/2} Q^{-1/2}$, $v \sim \kappa Ra^{1/2} L^{-1} Q^{-1}$ for the top and bottom Ekman layers to be compatible.

Figure 2 is a schematic diagram of the variation of stream function, azimuthal velocity interior buoyancy and heat flux as Q varies, and is intended as a summary of the above qualitative statements based on scaling arguments.

The majority of the equations in the foregoing remain intrinsically nonlinear and therefore, intractable. To add to the difficulty, there are vertical side-wall layers present on $x = 0$ and $x = L$. We have seen that fluid at the hot end ($x = L$) rises in a thin side-wall layer which also becomes homogeneous above the thermal layer (the non-rotating arguments given by Killworth & Manins 1980, to show homogeneity still hold in the rotating case). The fluid is distributed laterally in the top Ekman layer and pumped back into the interior as a downward vertical velocity. Hence the side-wall layer on the cold wall ($x = 0$) must be passive, serving only to bring w to zero. Killworth & Manins' argument shows that ψ must vanish at the interior edge of this layer (and so, from (3.1), must v).

However, the side-wall layer at $x = L$ permits of no such facile analysis. It must

bring the interior v and w (both independent of z) to zero; there is no interior u velocity, and the fluid is homogeneous. Surprisingly, the Rossby number of the flow in each regime is too high to permit a traditional linear $E^{\frac{1}{2}} - E^{\frac{1}{2}}$ layer structure (the balance being (for example) $G \sim I$ and thus nonlinear). We are forced to assume (at least for the similarity solution of §5) that this side-wall layer(s) resembles its linear counterparts, which can indeed bring v and w to zero, and is a passive part of the dynamics.

There is support for this assumption in the strong and very strong rotating cases. Stern (1975) was able to solve the interior and bottom layer problem without solving the side-wall layers (which were indeed passive); Daniels (1976) discussed the side-wall layers for very strong rotation, and these too do not affect the interior solution. It is thus plausible that the side-wall layers never affect the problem; but, as these are nonlinear, confirmation is lacking.

The side-wall layers are still more complicated in the corner region $x \sim L, z \sim L Ra^{-\frac{1}{2}}$. Provided that $u > 0$ away from the corner, the predominant balance for ψ is advective-diffusive, as in the non-rotating case (Killworth & Manins 1980). v and Δ are quite passive, being advected and diffused by the ψ field, so that the layer has only to accept the interior ψ field. The layer widens from $L\sigma Ra^{-\frac{1}{2}}$ to $L Ra^{-\frac{1}{2}}$ as u becomes smaller, so that horizontal friction re-enters the balance, and appears to remain this thickness for $u < 0$. Again, the dynamics of the layer are nonlinear, and our belief that the side-wall layer is passive is based on the Stern and Daniels solution.

Finally, we should note some typical parameter values. For the experiments the data of §2 indicate maximum Rayleigh numbers of $\approx 2 \times 10^8$ ($\pm 2\%$) for water and $\approx 7.5 \times 10^8$ ($\pm 12\%$) for paraffin. Similarly for water $E \lesssim 5 \times 10^{-4}$ and for paraffin $E \lesssim 9 \times 10^{-4}$ with an uncertainty of 5%. Thus $E^{\frac{1}{2}} \sim Ra^{-\frac{1}{2}} \ll 1$, implying that $Q \sim 1$, which corresponds to the medium rotation regime. The range over which Q could be varied was ≈ 0.3 to 3 for paraffin (uncertainty 7%) and ≈ 1 –10 for water (uncertainty 1%). This range borders on weak rotation at the lower end and strong rotation at the upper.

4. Experimental results

(a) General characteristics

It quickly becomes clear during the experiments that for both rotating and non-rotating flows the essential features were similar to those observed by Rossby, i.e. an approximately isothermal interior surmounting a strongly stably stratified thermal layer over the colder part of the base, and an area of static instability over the warmer part of the base feeding into a narrow region of rising motion up the outer wall. In the rotating case this fluid then enters an Ekman layer on the lid, which is in contact with the fluid. In agreement with Miller (1968) time-dependent motions with periods of order the rotation period were observed in this unstable region; it is thought these can be attributed to the release of thermals.

As in the side-wall-heated annulus, for a given temperature difference, there is a critical rotation rate above which there exists a wave regime; flow visualization indicated that these waves drifted relative to the annulus, took up an integral number of lobes around the annulus and were characterized by a jet-stream type of flow. The perturbation to the velocity field extended throughout the depth of the fluid but temperature fluctuations were restricted to the thermal layer. The transition to the

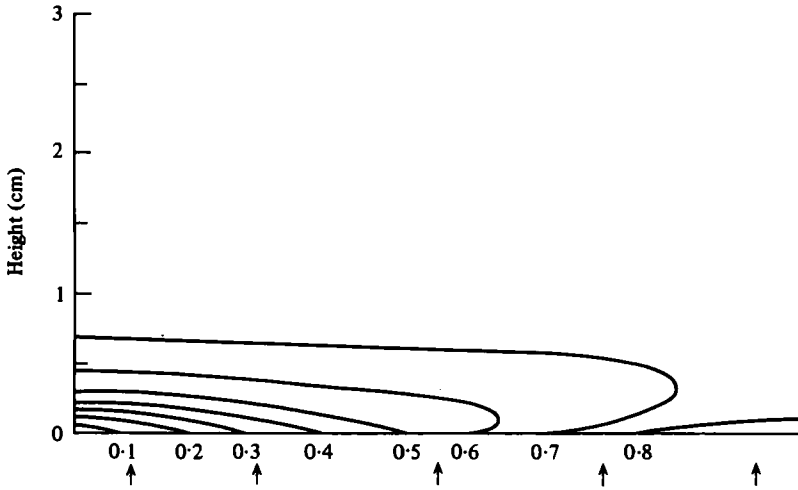


FIGURE 3. A radial temperature cross-section at $Q = 0$, $Ra = 2.34 \times 10^8$, working fluid water, $d = 10.0$ cm. The isotherms are expressed as fractions of ΔT and were drawn subjectively from vertical temperature profiles at the arrowed positions. The gradients above about 1 cm are too weak to include.

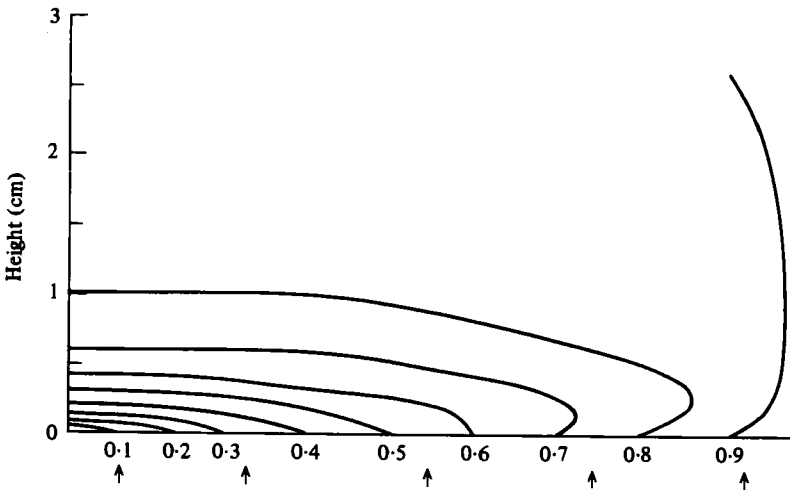


FIGURE 4. As for figure 2 except $Q = 2.88$, $Ra = 2.38 \times 10^8$, $E = 1.55 \times 10^{-4}$, working fluid water. Note the slight deepening of the thermal layer and the increase of the interior temperature from $Q = 0$.

wave regime was arbitrarily defined as occurring when the maximum peak-to-peak amplitude of the temperature fluctuations exceeded $0.01\Delta T$ as determined from a thermocouple in the centre of the gap width. On this basis it appeared that for both fluids at $Ra > 10^8$ a single critical value of Q was appropriate, viz. $Q_c = 3.4$, with an uncertainty of about 10%. A few experiments were carried out with varying geometry. With the existing gap width the depth was progressively reduced to 3 cm without any discernible change in Q_c . A larger inner cylinder was introduced to give $(b - a) = 5$ cm; at unity aspect ratio Q_c was reduced to ≈ 1 . It is difficult to make direct comparisons here, since Ra was necessarily reduced to $\approx 10^5$, but it is interesting to note that still $Q_c \sim 1$.

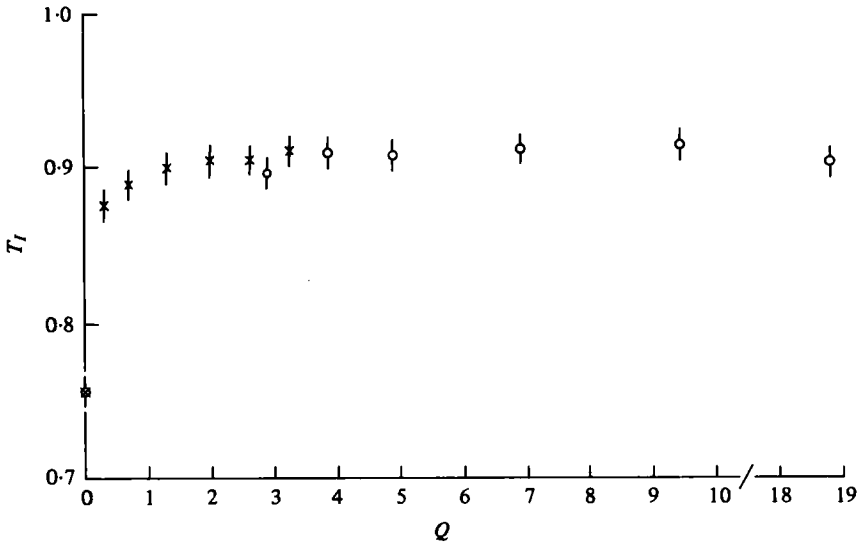


FIGURE 5. A normalized interior temperature T_I versus Q ; note the break in scale at large Q . Crosses denote paraffin at $Ra \approx 7.5 \times 10^8$ and circles water at $Ra \approx 2.4 \times 10^8$.

Concentrating now on steady, axisymmetric flows, radial cross-sections of the temperature field are presented in figures 3 and 4 for values of $Q = 0$ and $Q = 2.88$ respectively; both cases are for water at essentially the same Rayleigh number. The isotherms are expressed as fractions of ΔT and only the bottom third of the annulus is shown in detail, the gradients above this being very weak. The figures were compiled from vertical temperature profiles made by the five thermocouples with measurements at ten levels in the bottom 0.5 cm and a total of twenty throughout the entire depth. Figure 3 is comparable with Rossby's experiments, although the geometry is different, specifically the curvature and a higher aspect ratio ($= d/(b-a)$). In particular the interior temperature is seen to lie between 0.7 and 0.8 of ΔT . In figure 4 it can be seen that the thermal layer is thicker and the interior is significantly warmer than the non-rotating case. To examine this latter feature a quantity T_I was defined as the mean temperature recorded by the central three thermocouples in the upper half of the fluid and expressed as a fraction of ΔT . Figure 5 displays T_I versus Q for the maximum Ra attainable with both water and paraffin, i.e. $\approx 2.4 \times 10^8$ and $\approx 7.5 \times 10^8$ respectively; note the break in the abscissa at the highest values of Q .

There is clearly a significant rise in T_I as Q increases from zero. Apparently a maximum of ≈ 0.9 is reached by $Q = 3$ with no obvious sign of steady increase to $T_I = 1$ at large Q .

(b) *Structure of the thermal layer*

A characteristic of the thermal-layer structure is that horizontal temperature gradients are much less than the vertical gradients, which implies that a possible balance would be between vertical advection of heat and vertical diffusion, at least over a limited area not too close to the base where horizontal advection can be expected to be of importance; i.e. the heat equation can be simplified to

$$wT_z = \kappa T_{zz},$$

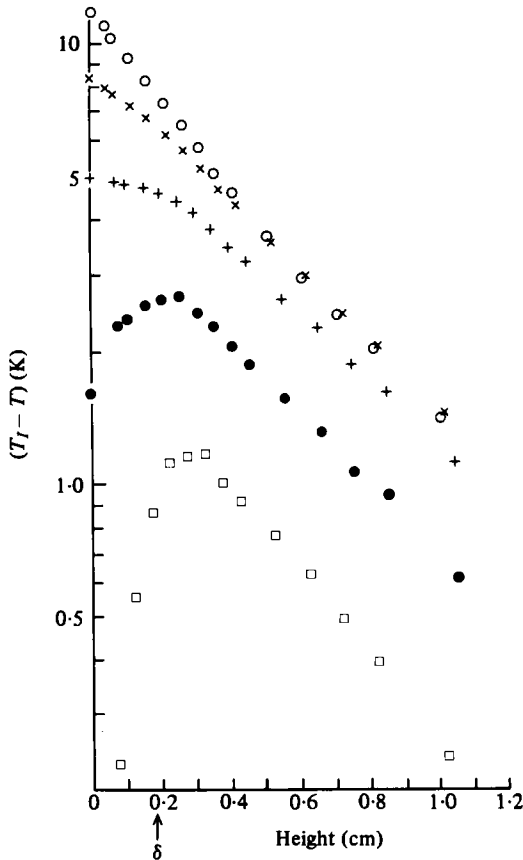


FIGURE 6. $(T_I - T)$ versus height at $Q = 2.88$ at five radial positions: \circ , I; \times , II; $+$, III; \bullet , IV; \square , V. A negative gradient implies sinking motion; a positive gradient rising motion. Errors will be largest close to the base near the inner cylinder, typically ± 0.2 K, although here values may be shifted slightly toward interior values because of probe effects.

a solution of which can be written as

$$T(r, z) = T_I - (T_I - T(r, 0)) \exp(-z/h(r)),$$

where $h(r) = -\kappa/w(r)$ is a scaling length and provided that w is independent of height. The results of plotting $\ln(T_I - T)$ against height at each of the five radial positions for a typical value of Q ($= 2.88$) are shown in figure 6. Only one example is presented here but each value of Q demonstrated the same features over the range examined, including time-averaged profiles obtained in the wave regime. Close to the inner cylinder the gradient is negative and approximately linear almost to the base; a negative gradient represents sinking motion. On moving radially outwards the profiles deviate from the linear section as they approach the base; both the magnitude of this deviation and the height at which it occurs increase with radius until the gradient reverses and the statically unstable region of rising motion is encountered. The linear sections of the curves can be seen as regions of limited vertical extent in which vertical heat advection closely balances vertical diffusion; above this there is an advective interior and below it, adjacent to the base, it would seem reasonable at this stage to assume that horizontal

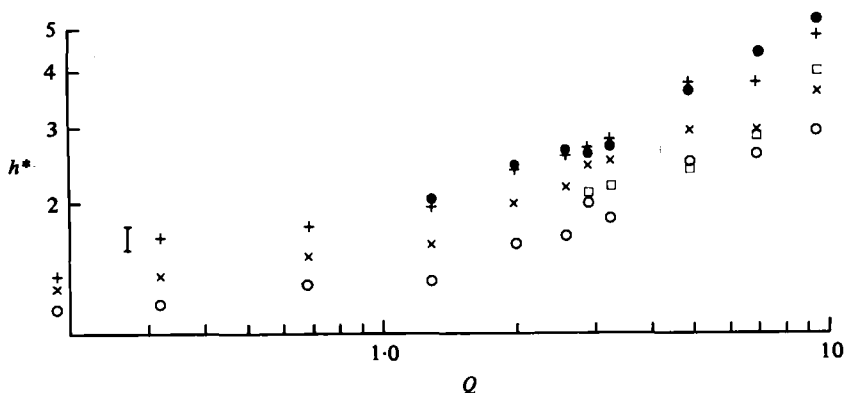


FIGURE 7. Scaled thermal layer thickness versus Q ; $h^* = h/(b-a)Ra^{-\frac{1}{2}}$; symbols; as in figure 6. Values for $Q = 0$ are shown on the left.

advection is important in the heat balance, since as the fluid moves outwards across the base, warming as it does so, the deviation from the simple vertical balance becomes increasingly large.

The linear sections of figure 6 have a slope of $-h^{-1}$. The scaling analysis of § 3 suggests that a measure of the thermal-layer thickness should remain almost independent of Q for $Q < 1$. With this in mind values of h were inferred for values of Q over the range 0–9.42, for all five radial positions, from the gradients of those sections which were judged, by eye, to be approximately linear. Although this is a subjective procedure it seemed to be the most straightforward way of delineating those regions in which the simple vertical balance held. A scaled layer thickness $h^* = h/(b-a)Ra^{-\frac{1}{2}}$ was computed and is plotted in figure 7 against Q on a log diagram. Values of h^* at the outer radial positions are not shown for small Q since here the extent of the simple vertical balance was too limited to allow reliable estimates of h to be made; the appropriate values for $Q = 0$ are shown on the left. It can be seen that certainly for points over the stably stratified section there is a slow increase of h^* with Q until $Q \approx 1$, above which there is a more rapid variation. The radial variation of h^* shows a broad maximum rather more than half-way across the annulus with a marked reduction on approaching the outer wall, implying an increase in the vertical velocity. For clarity a single representative error bar is shown, although points at the three highest values of Q may be subject to larger errors due to inadequate sampling of the waves.

(c) Some aspects of the velocity field

Flow visualization indicated that typical azimuthal velocities in the symmetric flow were relatively slow, at most $\approx 1 \text{ mm s}^{-1}$. This, combined with the near-isothermal state of much of the fluid, indicates some of the problems which may arise when attempting to maintain insulating boundary conditions. A horizontal temperature gradient of only 0.025 K cm^{-1} represents, via the thermal wind equation for the parameters relevant to the $Q = 2.88$ case, a vertical shear of the azimuthal velocity of $\approx 0.08 \text{ mm s}^{-1} \text{ cm}^{-1}$ and this, if maintained over several centimetres, would be comparable in magnitude to typical velocities. Such an effect was observed near the inner cylinder in the upper half of the fluid and was probably driven by a slight heat loss of

less than 50 mW. It is believed, however, that this effect was localized to the immediate vicinity of the boundary.

The vertical shear of the azimuthal velocity component occurs, in the thermal layer, over a depth of several millimetres. Consequently reliable direct measurements in this region proved practically to be difficult and none of sufficient accuracy or resolution were obtained. It was therefore decided to deduce as much as was feasible about the velocity structure of the thermal layer from the temperature data taken at $Q = 2.88$ ($Ra = 2.38 \times 10^8$, $E = 1.55 \times 10^{-4}$, working fluid water) in the symmetric flow regime. The equations of motion in component form can be written for two-dimensional flow with no time dependence as

$$-2\Omega v = -p_r/\rho_0 + \nu u_{zz}, \quad (4.1)$$

$$2\Omega u = \nu v_{zz}, \quad (4.2)$$

$$\rho g = -p_z \quad (4.3)$$

where the hydrostatic approximation has been made, curvature terms have been neglected and ρ_0 refers to some basic reference state. After forming a complex variable $\eta = u + iv$, (4.1)–(4.3) can be combined into a single differential equation,

$$\eta_{zz} - i2\Omega\eta/\nu = 2\Omega(F + v_g)/\nu, \quad (4.4)$$

where v_g is the azimuthal velocity at some reference level at which the flow is geostrophic, and $F = g \int \rho_r dz / 2\Omega$ represents the contribution of the thermal wind in balancing a vertical shear of v . From the experimental data F was computed by interpolating between the temperature profiles. The choice of the reference level is somewhat arbitrary, but was most conveniently taken to be that at which $v = v_g = 0$, since this could be determined relatively easily by eye and is close to the top of the thermal layer, minimizing the vertical distance over which (4.4) must be integrated to give u and v as functions of height. This procedure was carried out midway between the thermocouple positions at $r = a + (0.16, 0.38, 0.61)(b - a)$. Of these terms neglected in the equations of motion it is estimated that inertial terms would not contribute to u and v by more than a few per cent and that in the overall balance curvature terms are at least two orders of magnitude less than the leading terms.

Direct measurements of the azimuthal velocity profile were made 9 cm above the base by analysis of successive dye streak photographs. These were then combined with the computed velocities to give a radial cross-section of the azimuthal velocity field, as shown in figure 8. This is incomplete in the region close to the outer wall, where there are insufficient data. Full lines are prograde, dotted lines retrograde and the contours are evenly spaced at intervals of 0.2 mm s^{-1} . In the upper part the azimuthal velocity increases almost linearly with radial distance from the inner cylinder and there is no significant vertical shear, except in the upper Ekman layer; a typical uncertainty in these values is about 10%. The maximum v of $\approx 0.9 \text{ mm s}^{-1}$ is reached about three-quarters across the gap width. In the thermal layer the velocity maximum is broader, reaches $\approx 0.7 \text{ mm s}^{-1}$ and occurs near the centre of the gap width. However, the error on these inferred velocities is rather higher than the direct measurements and is essentially a systematic one. Given the amount of manipulation which the basic data have undergone an estimate of the worst-possible error in the magnitudes of these velocities would be $\approx 25\%$.

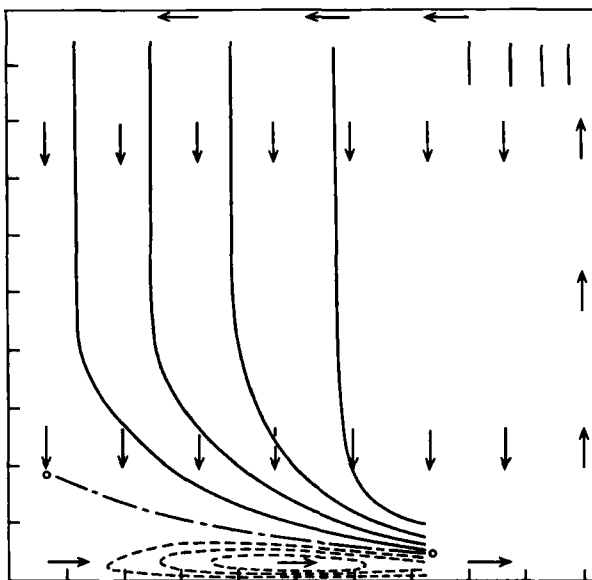


FIGURE 8. Radial cross-section of the azimuthal velocity field, as described in §4(c); full lines prograde, dotted lines retrograde, contour interval 0.2 mm s^{-1} . The arrows indicate the nature of the overall radial circulation.

The arrows in figure 8 indicate the form of the radial circulation, their length is not significant. Away from the outer wall there was no observable radial motion outside thin boundary layers on the base and lid. The radial flux at the lower boundary turns the corner at the outer edge of the base and rises up the outer wall. Now the outer profile of figure 7 ($\ln(T_1 - T)$ vs. z) indicates sinking motion at heights greater than a few millimetres above the base, implying that upward motion at the outer wall occupies less than 9% of the annular gap at this level. However, at the top of the outer wall the sign of the relative vorticity, as shown by the radial shear of the azimuthal velocity, is such that, by Ekman motion, the rising motion here occupies an area equivalent to about 30% of the annular gap, indicating a thickening of the plume as it rises up the wall.

There is now almost enough information to permit an examination of the heat balance of the thermal layer by computing the magnitudes of the vertical and horizontal advection terms in the heat equation; only w remains to be decided. If it be assumed that the vertical velocity has the Ekman layer variation the dependence of w on height can be written as

$$w = w_1(1 - \exp(-z/\delta))(\cos z/\delta + \sin z/\delta),$$

where $w_1 = -\kappa/h$. Hence values of u , to give $u \partial T / \partial r$, were interpolated from the above velocity analysis and $w \partial T / \partial z$ was evaluated from the basic temperature profiles. The variation of these quantities with height is shown in figure 9(a), (b) for positions close to the inner cylinder and halfway across the gap width. As in the velocity calculations the error here is essentially a systematic one, i.e. the shape of the profile is known, also the boundary value (zero) and, with lesser confidence, the interior value. Hence a single error bar is used to indicate the worst error in the maximum values.

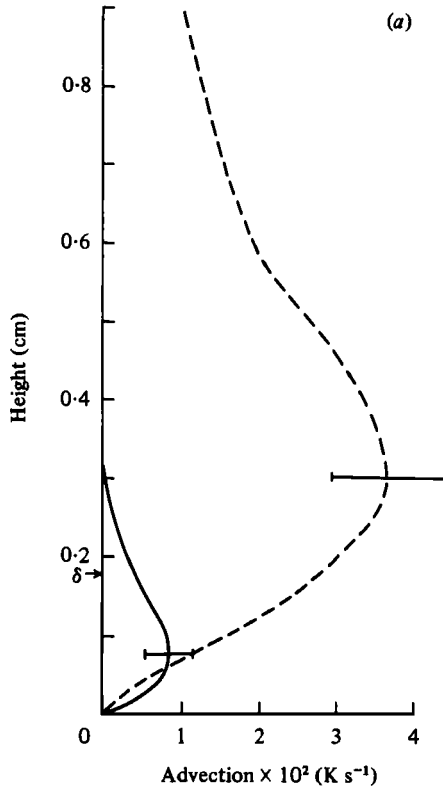


FIGURE 9(a). For the caption see next page.

Figures 9(a), (b) illustrate the correct interpretation to be placed on the profiles shown in figure 7, of $\ln(T_I - T)$ vs. z . Close to the inner cylinder vertical advection dominates over horizontal almost to the base; as the fluid moves outwards horizontal advection becomes increasingly important and accounts for the tendency of the profiles in figure 7 to curve away from linear near the base. The point at which this deviation occurs corresponds closely to the height at which there is a change in the dominant term in figure 9(a), (b). Furthermore this point indicates the position of a maximum in the vertical temperature gradient; $\partial^2 T / \partial z^2$ must change sign here since it is vertical diffusion which is balancing the advection.

(d) *Heat-flux measurements*

It was hoped that the temperature measurements could be used to infer the heat flux by computing the vertical temperature gradients close to the base. However, it was found in practice that reliable results could not be obtained because, it is believed, of finite probe effects in the region of large vertical temperature gradients immediately adjacent to the base near the inner cylinder. However, since the completion of the rotating experiments, two non-rotating experiments in the same annulus have been completed using a single thermocouple probe in which the leads are introduced horizontally to minimize errors caused by conduction of heat along the wire. Using the motor-driven probe positioner the vertical gradients were evaluated at the base and from these measurements the Nusselt number was expressed as $Nu = kRa^{-\frac{1}{2}}$, where

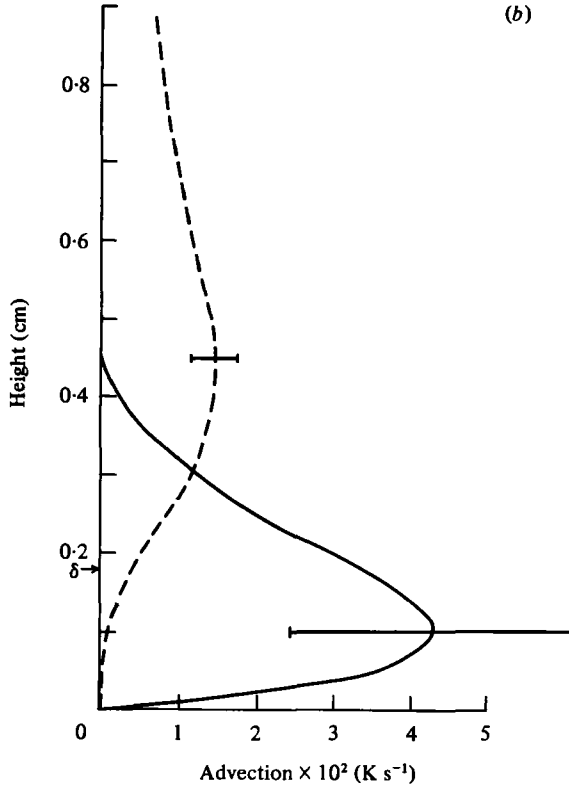


FIGURE 9. Horizontal and vertical advective terms for $Q = 2.88$ at (a) position I and (b) position III. Full lines are $u \partial T / \partial r$ and dotted lines $-w \partial T / \partial z$.

$k \approx 0.2$ for water and paraffin, with an uncertainty of 15%. This value is in very good agreement with the result obtained by Killworth & Manins (1980) for a cell of unity aspect ratio. It is hoped that more comprehensive measurements of the heat flux will form part of future work.

5. The similarity solution

The equations describing the flow regimes mentioned in §3 are, for the most part, highly nonlinear partial differential equations, and little progress can be made in their solution. However, when the base buoyancy distribution is quadratic in x , there exists a similarity solution in the non-rotating case (Duncan 1966; Killworth & Manins 1980). This can be extended to the rotating problem, to allow some quantitative comparison with observations. This similarity solution, as noted by Killworth & Manins, is a special case of the solution of Duncan (1966).†

The solution has

$$\psi \sim xf(z), \quad \Delta \sim x^2g(z) + k(z), \quad v \sim xh(z), \quad (5.1a,b,c)$$

and requires the base buoyancy distribution $\Delta_0(x) = \Delta_m(x/L)^2$. It trivially satisfies all

† The comments concerning the side-wall layers in §9 should be recalled. We reiterate our belief that these layers are passive, but know of no proof except in the limit $Q \gg 1$.

boundary conditions on $x = 0$, and, provided $k(z)$ is suitably adjusted, gives a steady solution with no net heat flux into the system.

The equations which are produced by substitution of (11.1) into (3.1) to (3.3) are still nonlinear, and usually stiff (i.e. they possess growing and decaying solutions over two or more length scales differing by an order of magnitude). This presents problems numerically; the only reliable solutions were found in the range $0.1 \leq Q \leq 3$, which is verging on weak rotation at the lower end, and strong rotation at the upper. Outside this range rounding and truncation errors dominate the solution. However, this range spans the steady flow found experimentally.

Using the scaling for the medium rotation regime (neglecting nonlinear momentum terms, therefore), the relevant equations are (3.4)–(3.6). So, writing non-dimensionally (and now using the stretched variable ζ),

$$\psi = xf(\zeta), \quad \Delta = x^2g(\zeta) + k(\zeta), \quad v = xh(\zeta), \quad (5.2a,b,c)$$

gives

$$g'' = 2f'g - fg', \quad k'' = -fk', \quad h'' = Qf', \quad f^{iv} = 2g - Qh', \quad (5.3a,b,c)$$

where a prime indicates differentiation with respect to ζ , and with boundary conditions

$$f = f' = h = g - 1 = k = k' + \frac{1}{3}g' = 0, \quad \zeta = 0, \quad (5.7)$$

$$g \rightarrow 0, \quad f \rightarrow f_\infty, \quad k \rightarrow k_\infty, \quad h \rightarrow h_\infty = 2\frac{1}{3}f_\infty, \quad \zeta \rightarrow \infty, \quad (5.8)$$

where f_∞, k_∞ are (unknown) asymptotic values, h_∞ is required by the familiar Ekman consistency condition at the lid and the condition on $k'(0)$ is obtained from the requirement that no net buoyancy flux enters or leaves the fluid, as

$$0 = \int_0^1 \Delta_\zeta(x, 0) dx = \int_0^1 \{x^2g'(0) + k'(0)\} dx = \frac{1}{3}g'(0) + k'(0). \quad (5.9)$$

These equations were solved numerically, using the Taylor system (Norman 1972), although other methods were tried, particularly stiff system solvers. As noted above, solutions well into the weak or strong rotation regimes could not be found (except, of course, by assuming the very balance which the similarity solution was designed to test).

Solutions for $Q = 0.1, 1$ and 3 are shown in figures 10, 11 and 12 (note the $Q^{-\frac{1}{2}}$ factor on h , for plotting convenience). When Q is small (0.1) the division between the inner buoyancy layer ($\zeta < 3$, say), and the outer, homogeneous Ekman layer, is clearly marked. The thickness of the Ekman layer is, in this scaling, $(2/Q)^{\frac{1}{2}}$, or 4.5 , so that, by $\zeta = 9$, the interior asymptotics have not been reached. Increasing Q to 1 (figure 11) approximately superimposes buoyancy and Ekman layers, so that the familiar Ekman spiral is modified by buoyancy effects. When Q is 3 (figure 12), the Ekman spiral is confined to $\zeta < 3$, with an outer buoyancy layer in 'thermal wind' balance which is again decaying slowly with ζ (as indicated by the strong rotation scaling).

The way in which interior quantities change with Q is shown in figures 13 and 14. Figure 13 shows the variation of f_∞ (i.e. $\psi_I/(x\kappa Ra^{\frac{1}{2}})$) with Q ; v decreases monotonically with Q over the range studied. Also shown are the asymptotes for weak and strong rotation. These may be obtained, briefly, as follows. For weak rotation, §3 showed that the lower Ekman layer must bring ψ and v to zero, while the thermal layer below it satisfies the non-rotating equations (with a much reduced ψ , however). Hence, for the

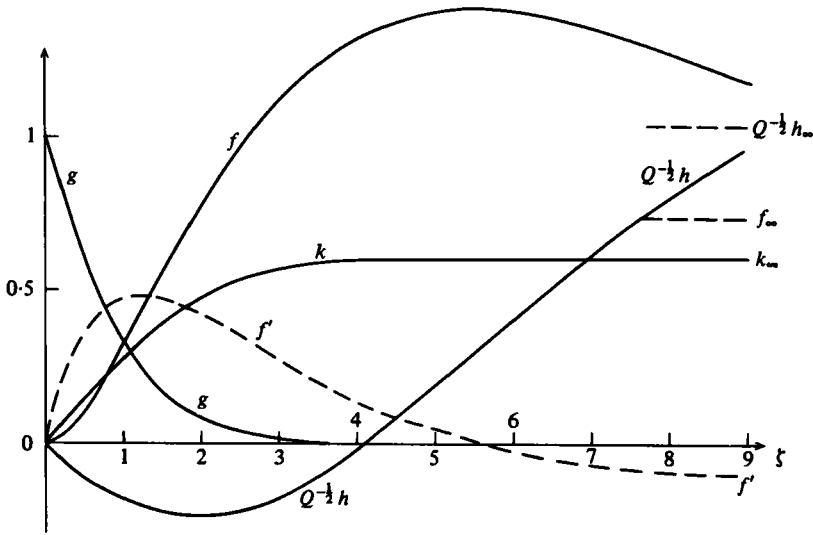


FIGURE 10. Solutions to the similarity equations (5.3) to (5.6) for the low rotation case $Q = 0.1$. Note that $Q^{-1/2}h$, and not h , is plotted for convenience.

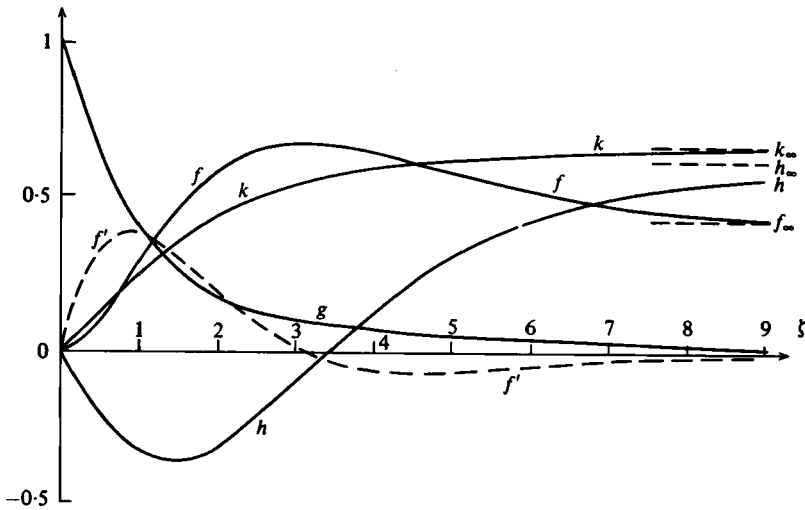


FIGURE 11. As figure 10, but for $Q = 1$.

thermal layer, we must have $\psi \rightarrow \psi_1(x) + \zeta\psi_2(x)$ as $\zeta \rightarrow \infty$ for some functions $\psi_1, \psi_2(x)$. Matching ψ_2 at the base of the Ekman layer yields

$$f_{\infty} x \sim \frac{\psi_2(x)}{2^{1/2} Q^{1/2}}. \tag{5.10}$$

From Killworth & Manins (1980), $\psi_2(x) \sim 0.638x$, giving

$$f_{\infty} \sim 0.23Q^{-1/2}, \quad Q \rightarrow 0, \tag{5.11}$$

until the very weak regime is attained. Ekman compatibility then yields

$$h_{\infty} \sim 0.638/2 \sim 0.32, \quad Q \rightarrow 0. \tag{5.12}$$

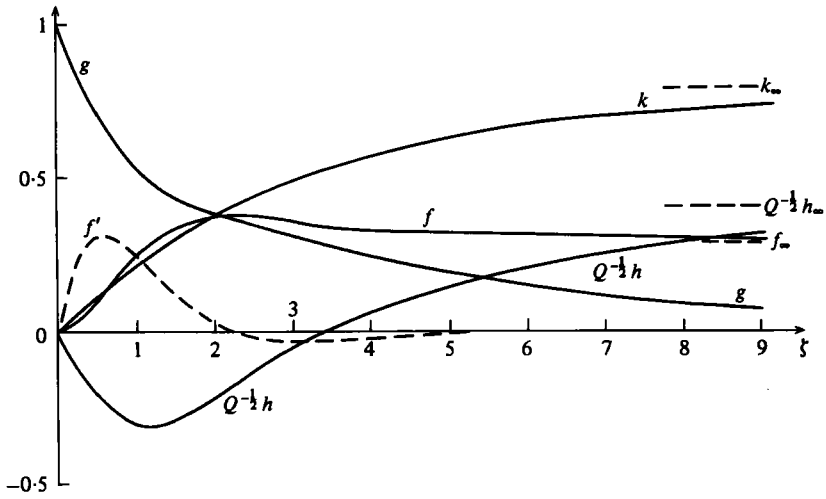


FIGURE 12. As figure 10, but for $Q = 3$.

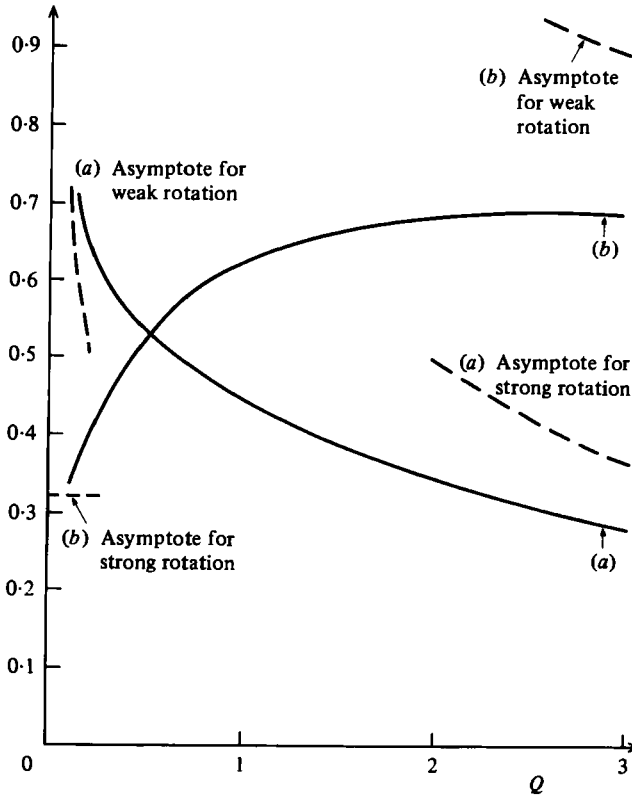


FIGURE 13. Variation of interior quantities with Q for the similarity solution: (a) stream function $\psi/(x\kappa Ra^{1/2})$; (b) azimuthal velocity $vL/(x\kappa Ra^{1/2})$. Asymptotes for weak and strong rotation are also shown.

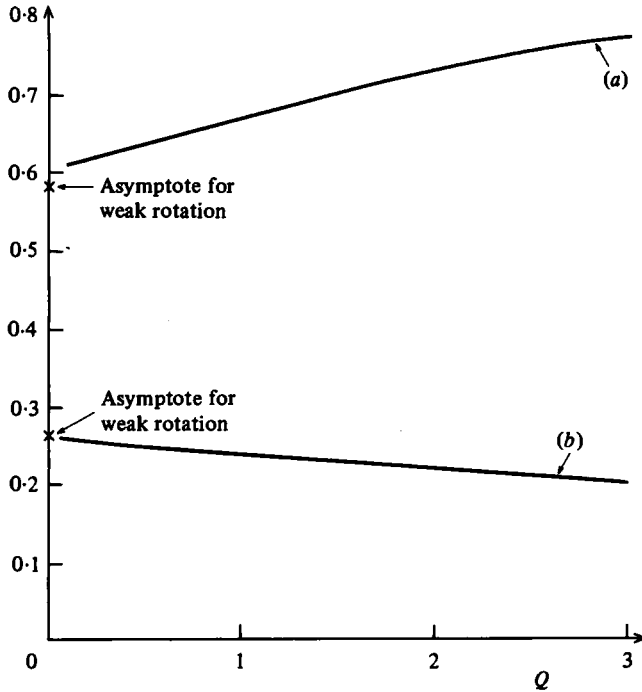


FIGURE 14. Variation with Q for the similarity solution of (a) the abyssal buoyancy, $k_\infty (= \Delta_I)$ (b) the heat flux $NuRa^{-1/2}$. The low Q asymptotes are also shown.

For strong rotation it is necessary to solve equation (12.2.14) of Stern (1975), or an equivalent second-order differential equation for the interior transport, for $\Delta_0(x) = x^2$. This yields a solution of the similarity form, with

$$f_\infty \sim 2^{-1/2} Q^{1/2}, \quad Q \rightarrow \infty, \tag{5.13}$$

and, from Ekman compatibility,

$$h_\infty \sim 2^{1/2} Q^{-1/2}, \quad Q \rightarrow \infty. \tag{5.14}$$

It is clear from figure 13 that $Q = 0.1$ is just entering the weak rotation regime, but that $Q = 3$ has not yet reached the strong rotation regime, although v has reached a maximum at about $Q = 2.8$.

Figure 14 shows how k_∞ (i.e. Δ_I) varies with Q . In agreement with figure 5, it increases monotonically with Q . For small or zero Q , $\Delta_I \approx 0.58$, as found by Killworth & Manins (1980), but the rate of increase of Δ_I is far weaker than observed. The absolute change in Δ_I , however, from $Q = 0$ to 3, is about 0.2, comparing well with the 0.15 change found over the same range experimentally. Apart from the differences in absolute values in Δ_I (attributable, as Killworth & Manins (1980) note, to the different $\Delta_0(x)$ behaviour between theory and experiment), the different rates of increase may be caused by our neglect of curvature effects. Finally figure 14 also shows the variation of Nusselt number with Q ; the asymptote for small Q is that for the non-rotating case. There are no direct measurements in the rotating flows to allow comparison.

Also presented are two diagrams which allow some direct comparison of the flow with observations. Figure 15 shows the magnitudes of the terms in the buoyancy

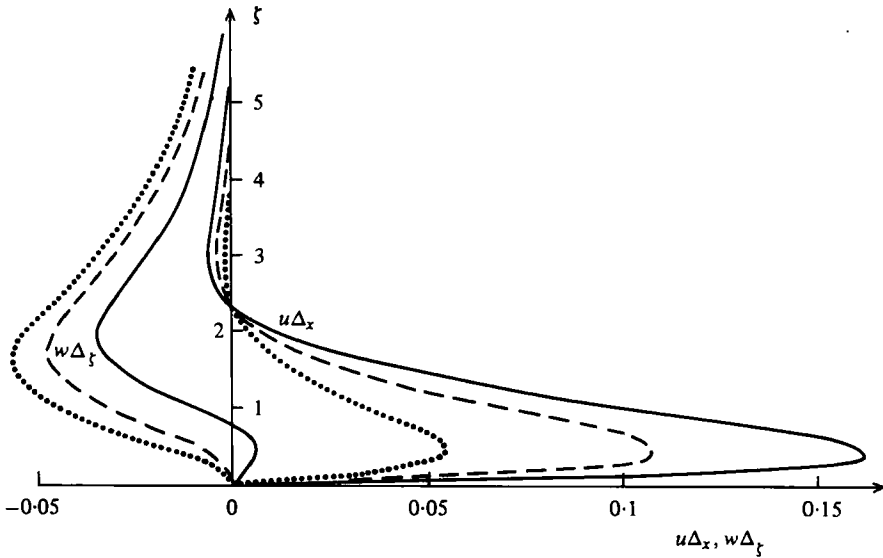


FIGURE 15. Advective term balance in the buoyancy equation for the similarity solution, for $Q = 2.8$. —, $x = 0.75$; ---, $x = 0.5$; ..., $x = 0.25$.

equation as functions of ζ for $Q = 2.8$, at three values of x across the annulus. These may be compared with observational values in figures 9 (*a, b*). There is good qualitative agreement and surprisingly good quantitative agreement in view of the simplifications involved. For example, at the centre of the gap width, figure 15, in dimensional form, gives values for the maxima in $u\partial T/\partial r$ and $-w\partial T/\partial z$ of ≈ 0.05 and $\approx 0.02 \text{ K s}^{-1}$ respectively at heights of $\approx 0.1 \text{ cm}$ and $\approx 0.35 \text{ cm}$. These agree very favourably with those shown in figure 9 (*b*).

6. Effects of baroclinic instability

For all values of Q , there are regions in the annulus where the fluid is statically unstable, i.e. Δ_z is positive. For regimes up to and including strong rotation, these regions are confined to a small part of the buoyancy layer (cf. figure 16). For very strong rotation, statically unstable fluid can typically occupy half the volume of the annulus (Daniels 1976).

Such statically unstable fluid is clearly a powerful source of available potential energy for small perturbations to the steady systems previously discussed, in addition to the normal sources of energy provided by the horizontal buoyancy gradients. For sufficiently large rotation rate, we should then expect a transition from a steady flow to a regular wave regime, rather as in more traditional annulus experiments (cf. Hide & Mason 1975). Observationally this variation occurs at values of Q of order unity. Hence the strong and very strong rotation regimes are unlikely ever to occur experimentally.

The existence of statically unstable fluid complicates the normal annulus criteria for instability. The requirement that the potential vorticity gradient change sign (it is independent of depth beyond the Ekman layer, as both Δ and v decay at the same rate with z) and the requirement that La^{-1} be sufficiently large, where a is the internal deformation radius, can both be written in the form $Q > Q_c$, for some critical value depending on the Prandtl number, length scales, and so on.

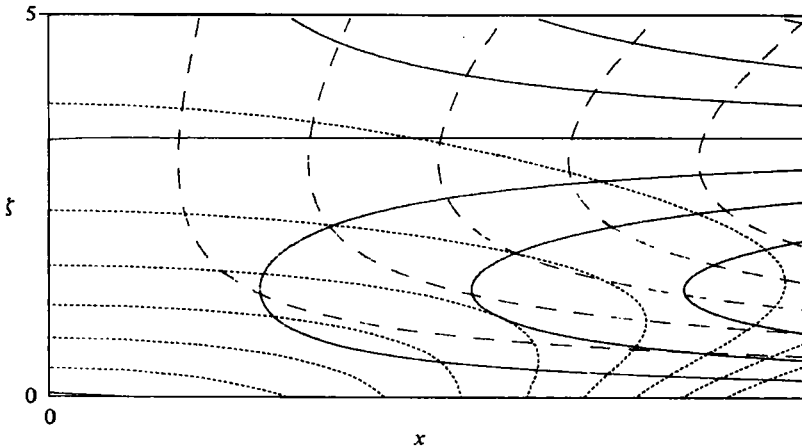


FIGURE 16. Contours of ψ , v and Δ in (x, ζ) space for $Q = 1$. The dashed lines (---) are equally spaced streamlines, returned upwards by a side-wall layer on $x = 1$. The dotted lines (...) are equally spaced isopycnals. Firm lines are equally spaced contours of v .

This suggests that transition to a wave regime occurs for Q greater than some Q_c . Experiments confirm this: $Q_c = 3.4 \pm 0.4$ for $Ra > 10^8$ with little observed variation with σ (although σ could not be varied over a wide range).

The effects of the waves appear to remove most of the predicted behaviour for strong rotation. We shall examine only averaged observational values in what follows. It appears that Δ_T is almost independent of Q once waves occur, whereas it seems likely that $\Delta_0(L) - \Delta_T$ should decay as $Q^{-\frac{1}{2}}$ approaching the strong rotation regime. It thus appears that part of the effect of instability is to trap more buoyant fluid near the floor, and so reduce Δ_T . This can be considered as a stabilizing (i.e. energy-dissipative) adjustment to the strong rotation case which would occur in the absence of instability. By reducing Δ_T , the horizontal buoyancy gradient at levels above $z' = 0$, which would otherwise run from zero to $\Delta(L, z') = \Delta_0(L)$, is now reduced to run from zero to a value at $x' = L$ which is less than $\Delta_0(L)$. This is a removal of some available potential energy in order to drive the instability.

A full theoretical study of the instability would involve a complicated numerical scheme; sufficient grid points to resolve the thin side-wall layers make such a study unfeasible. However, in the past much useful information has been gleaned from linear stability analyses of idealized basic flows, as exemplified by Hide (1969) who, in a discussion of the side-wall heated annulus problem, considered the properties of a zonal flow with a linear vertical shear, in 'thermal wind' balance, with the addition of upper and lower Ekman layers and/or sloping end-walls. Similarly, here an idealized model of interior azimuthal flow is studied. Fuller details may be found in Hignett (1979); only a summary is given here.

The strong rotation regime is represented by a layer of uniform flow, overlying a layer with constant shear and much higher stratification. The fluid is bounded above and below at $z = h$ and $z = -H$, with side walls at $y = \pm \frac{1}{2}$, and is unbounded in the x direction. The lower layer, in thermal wind balance, has a uniform vertical shear of magnitude U/H and constant buoyancy frequency N (taken as positive, where $N^2 = +\Delta_z$). The upper layer has a uniform flow U and constant buoyancy frequency n

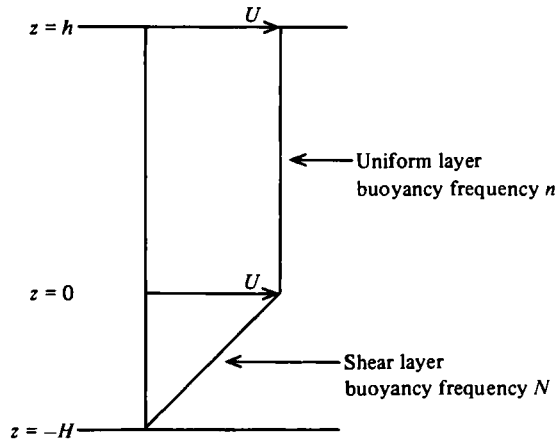


FIGURE 17. Schematic of model stability system, see §6.

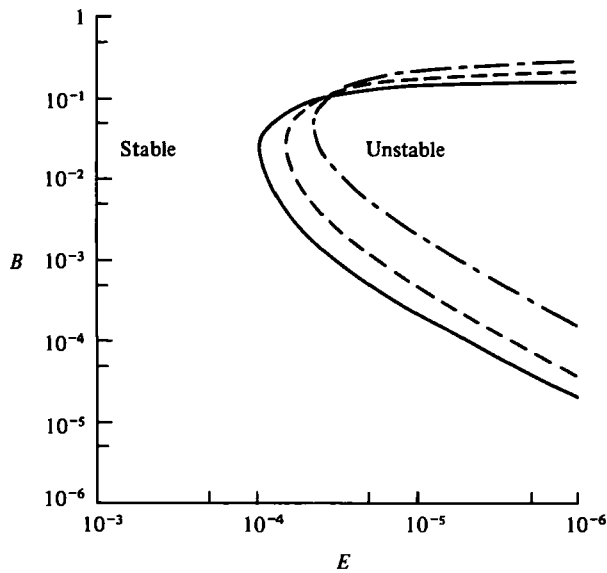


FIGURE 18. Marginal stability curve for $R = 10$ for model instability system, §6. —, $\mu = 0.15$, ----, $\mu = 0.5$; - · - · -, $\mu = 1.0$.

(as in figure 17). The inviscid problem was studied by Tang (1975); here Ekman layers are added on the upper and lower boundaries (cf. Barcilon 1964; Hide 1969).

The derivation of the quasi-geostrophic equations, their boundary conditions and jump criteria across $z = 0$ are well known and will not be repeated. If a perturbation proportional to $\exp ik(x - ct)$ is assumed, the eigenvalue problem yields a complex cubic equation for c (we assume the gravest mode in the y direction). The coefficients of this equation are functions of wavenumber, U , the Ekman number E (based, as before, on the length L), and the quantities

$$B = \left(\frac{NH}{fL}\right)^2, \quad \mu = \frac{H}{h}, \quad R = \frac{N}{n}. \tag{6.1}$$

The first of these (the square of the ratio of radius of deformation to length scale) takes the approximate value, at the cold wall, of

$$B \approx \sigma^{-1} Q^{-1/2}. \quad (6.2)$$

A typically marginal stability curve ($c_i = 0$) for $R = 10$, $\mu = 0.1, 0.5, 1.0$ is shown in figure 18. The familiar anvil-shaped area of instability found by several other workers is obtained (cf. similar diagrams for the conventional annulus produced by Mason, 1975). The main effect of viscosity is a stabilization for large friction. Instability further requires B to take a value less than about 0.1. Experimentally, for $Q = 2.88$, in the centre of the annular gap $R \sim 7$, $\mu \sim 0.1$, $E \sim 1.6 \times 10^{-4}$, and $B \sim 0.1$. Given these values, and the observation that the wave transition has the same character as that known as 'upper symmetric' in the traditional annulus, it seems likely that the experiments were conducted around the upper transition in figure 18.

Similar confirmation is found by consideration of the shape of the eigenfunction in the vertical. Provided R is fairly large, the eigenfunction shows no tendency to decay in the vertical (i.e. it takes values of the same order at all levels), and has very weak phase changes with z above the interface. Experiments also showed significant wave velocities throughout the depth of the fluid, with no detectable phase change with height above the bottom boundary level.

Such analysis is clearly a very crude representation of the actual instability problem. However the measure of agreement, both qualitative and quantitative, suggests that at least part of the dynamics in the wave regime is being modelled adequately by this simple model. Most encouraging is the qualitative finding that B must be less than some critical value for instability, which yields, via (6.2), the requirement that Q be greater than some critical value, as observed.

7. Conclusions

The dynamics of a rotating fluid annulus differentially heated along a horizontal boundary have been described in terms of six different regimes determined mainly by the magnitude of a non-dimensional parameter Q , defined on the ratio of the non-rotating thermal (or buoyancy) depth scale to the Ekman-layer scale. The flow consists of one or more horizontal layers adjacent to the heated and cooled boundary, a vertical flow up the side wall at the warm end of the base, and an almost neutrally stratified interior circulation. Side-wall and top layers complete the picture. Experiments have been carried out for values of Q of order unity. Flow properties vary smoothly with Q and in agreement with the scaling analysis until $Q \approx 3.4$ when (baroclinic) instability sets in.

The equations of motion remain nonlinear partial differential equations in character, despite the many scaling simplifications that can be made. In the case of a quadratic imposed temperature field, the similarity solution of Killworth & Manins (1980) can be extended to include rotation, and, over the range for which solutions can be found, there is favourable agreement with observation.

In terms of the large-scale ocean circulation Q would be expected to be large, say $Q \approx 100$, which would lie in the strongly rotating regime. However, the regimes and scalings presented here, while complicated, apparently possess only a limited relevance to geophysical problems such as large-scale oceanic overturning, due to the lack of

three-dimensional effects. A closed basin forces azimuthal pressure gradients and therefore radial motion in the interior. Stern (1975) extended his analysis of the annulus problem to one for a closed basin and found no effect on the parametric dependence of the buoyancy-layer thickness. However, Pedlosky (1969), linearizing the problem about a basic, vertical density gradient, found side walls to be very important. It would be valuable, therefore, for future experiments to include the insertion of full radial barriers, to introduce the effect of a closed basin, and to examine the effect of baroclinic instability on the growth features of the flow, particularly the heat flux and buoyancy-layer depth.

The authors wish to thank Dr R. Hide for his continuing support of this work and all members of the Meteorology department at Reading University and the G.F.D. laboratory at the Meteorological Office who helped with the apparatus. Two of us (P. H. and P. D. K.) received financial support from the N.E.R.C. during this project.

REFERENCES

- BAKER, D. J. 1966 A technique for the precise measurement of small fluid velocities. *J. Fluid Mech.* **26**, 573–575.
- BARCILON, V. 1964 Role of Ekman layers in the stability of the symmetric regime obtained in a rotating annulus. *J. Atmos. Sci.* **21**, 291–299.
- BEARDSLEY, R. C. & FESTA, J. F. 1972 A numerical model of convection driven by a surface stress and non-uniform heating. *J. Phys. Oceanogr.* **2**, 444–455.
- BJERKNES, V. 1916 *Leipzig, Abh. Ges. Wins.* **35**, 29.
- DANIELS, P. G. 1976 Thermal convection in a differentially heated rotating fluid annulus. *Geophys. Fluid Dyn.* **7**, 296–330.
- DEFANT, A. 1961 *Physical Oceanography*. Pergamon.
- DUNCAN, I. B. 1966 Axisymmetric convection between two rotating disks. *J. Fluid Mech.* **24**, 417–449.
- FEIN, J. S. 1978 *Boundary layers in Homogeneous and Stratified-Rotating Fluids*. University Press of Florida.
- HIDE, R. 1969 In *The Global Circulation of the Atmosphere* (ed. G. A. Corby). London: Royal Met. Soc.
- HIDE, R. & MASON, P. J. 1975 Sloping convection in a rotating fluid. *Adv. Phys.* **24**, 47–100.
- HIGNETT, P. 1979 Experiments on thermal convection in a rotating fluid annulus, driven by non-uniform heating from below. Ph.D. dissertation, University of Reading.
- JEFFREYS, H. T. 1925 On fluid motions produced by differences of temperature and humidity. *Quart. J. Roy. Met. Soc.* **51**, 347–356.
- KILLWORTH, P. D. & MANINS, P. C. 1980 A model of confined thermal convection driven by non-uniform heating from below. *J. Fluid Mech.* **98**, 587–607.
- MASON, P. J. 1975 Baroclinic waves in a container with sloping end-walls. *Phil. Trans. R. Soc. Lond. A*, **278**, 397–445.
- MILLER, R. C. 1968 A thermally convecting fluid heated non-uniformly from below. Ph.D. thesis, M.I.T.
- NORMAN, A. C. 1972 A system for the solution of initial and two-point boundary value problems. *Proc. Ass. Comp. Mach. (25th Anniv. Conf., Boston.)*, pp. 826–834.
- PEDLOSKY, J. 1969 The linear theory of the circulation of a stratified ocean. *J. Fluid Mech.* **25**, 185–205.
- ROSSBY, H. T. 1965 On thermal convection driven by non-uniform heating from below. An experimental study. *Deep-Sea Res.* **12**, 9–16.
- SANDSTRÖM, J. W. 1908 Dynamische Versuche mit Meerwasser. *Ann. Hydr. Met.* **6**.

- STERN, M. E. 1975 *Ocean Circulation Physics*. International Geophysics series, vol. 19. Academic.
- STOMMEL, H. 1950 An example of thermal convection. *Trans. Am. Geophys. Un.* **31**, 553-554.
- STOMMEL, H. 1962 On the smallness of sinking regions in the ocean. *Proc. Nat. Acad. Sci.* **48**, 766-772.
- TANG, C. M. 1975 Stratified shear flows in the atmosphere and ocean. *J. Geophys. Res.* **80**, 1168-1175.